Supporting Information for

Shell-Mediated Control of the Surface Chemistry in Highly Stoichiometric Magnetite Nanoparticles

Gabriel C. Lavorato[a*], Aldo A. Rubert[a], Yutao Xing[b], Raja Das[c,d], Joshua Robles[e], F. Jochen Litterst[f,g], Elisa Baggio-Saitovitch[f], Manh-Huong Phan[e], Hariharan Srikanth[e], Carolina Vericat[a], Mariano H. Fonticelli[a*]

a. Instituto de Investigaciones Fisicoquímicas Teóricas y Aplicadas (INIFTA), Universidad Nacional de La Plata – CONICET, 1900 La Plata, Buenos Aires, Argentina.

b. Laboratório de Microscopia Eletrônica de Alta Resolução, Centro de Caracterização Avançada para Indústria de Petróleo (LaMAR/CAIPE), Universidade Federal Fluminense, 24210-346, Niterói, RJ, Brasil

c. Faculty of Materials Science and Engineering and Phenikaa Institute for Advanced Study (PIAS), Phenikaa University, Hanoi, 10000, Vietnam

d. Phenikaa Research and Technology Institute (PRATI), A&A Green Phoenix Group, 167 Hoang Ngan, Hanoi 10000, Vietnam

e. Department of Physics, University of South Florida, 33620 Tampa, FL, United States

f. Centro Brasileiro de Pesquisas Físicas, 22290-180 Rio de Janeiro, RJ, Brasil.

g. Institut für Physik der Kondensierten Materie, Technische Universität Braunschweig, 38106 Braunschweig, Germany

[*] gclavorato@inifta.unlp.edu.ar; mfonti@inifta.unlp.edu.ar

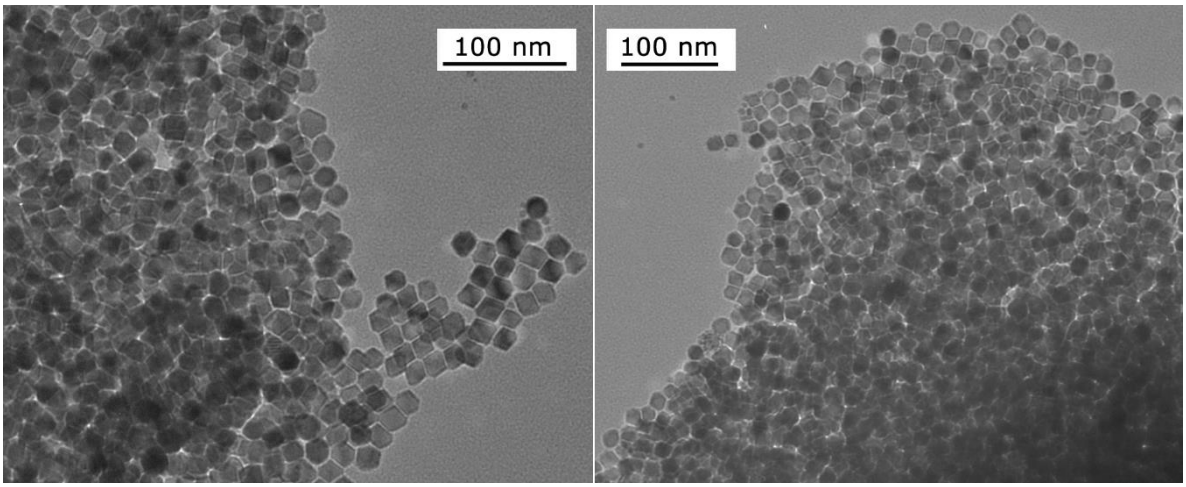

Figure S1 Additional TEM images of $Fe_3O_4/Zn_{0.6}Fe_{2.4}O_4$ core/shell nanoparticles.

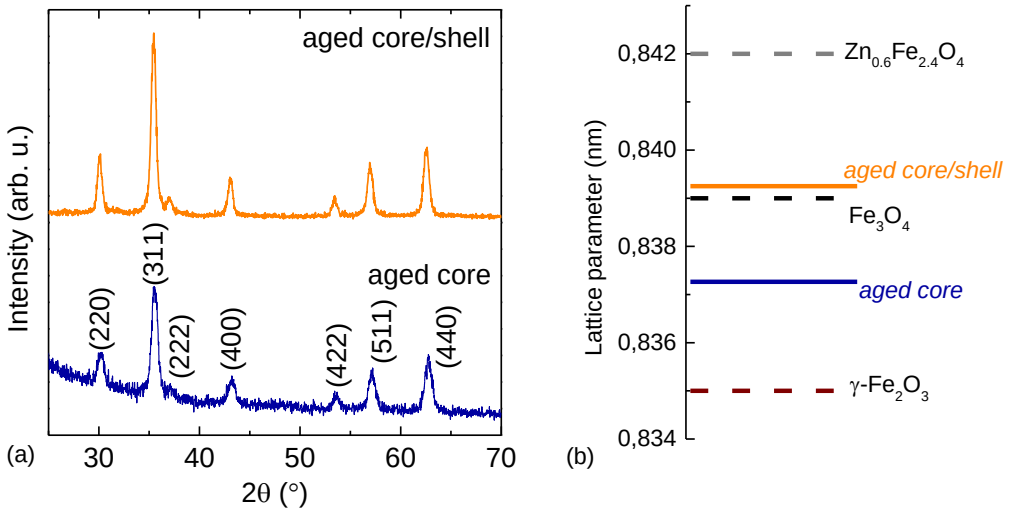

Figure S2 (a) X-ray diffractograms of 6-month aged bare cores and $Fe_3O_4/Zn_{0.6}Fe_{2.4}O_4$ core/shell nanoparticles and (b) comparison of the lattice parameters of the samples (solid lines) and selected bulk materials (dashed lines) from Ref [1]. The lattice parameter of $Zn_{0.6}Fe_{2.4}O_4$ is estimated according to the Vegard´s rule.

Mössbauer analysis

Table S1 Mössbauer parameters for the fits of the iron oxide cores room temperature spectrum shown in Figure 4: A (subspectrum area), S (isomer shift), B (magnetic hyperfine field), σ (Gaussian width of B), W (Lorentzian line width). Three sextets (S1-S3) were employed.

Sample	*Param.*	*S1*	*S2*	*S3*
cores	A (%)	24	28	48
	S (mm/s)	0.33	0.49	0.45
	B (T)	45.7	23.9	40.7
	σ (T)	1.2	10.0	4.7
	W (mm/s)	0.88	0.88	0.88

Table S2 Mössbauer parameters for the fits of the core/shell nanoparticles spectrum shown in Figure 4: A (subspectrum area), S (isomer shift), B (hyperfine field), σ (Gaussian width of B), W (Lorentzian line width). An additional divalent species (according to isomer shift) accounts for the 3% fraction of the total spectrum with a hyperfine field between 25 and 30 T. The number between parentheses is the estimated error.

	Shell		**Core**	
	Site A	Site B	Site A	Site B
A (%)	12(2)	43(2)	14(2)	28(2)
S (mm/s)	0.21(2)	0.57(2)	0.27(2)	0.65(2)
B (T)	47.2(2)	40.8(2)	45.1(2)	44.2(2)
σ (T)	0.8(2)	4.0(2)	0	0
W (mm/s)	0.22(5)	0.40(5)	0.50(5)	0.50(5)

Analysis of the magnetic properties

We considered the overall saturation magnetization for the core/shell NPs (M_S) from the contribution of the Fe_3O_4 core (M_F) and the Zn-ferrite shell (M_Z) weighted by their volumetric fraction (f): $M_S = M_F f_F + M_Z f_Z$. According to the TEM results, the magnetite (f_F) and Zn-ferrite (f_Z) fractions are about 0.35 and 0.65, respectively, and, due to its high crystallinity and stoichiometry, we can assume the low temperature literature value for M_F=98 emu/g [1]. This leads to the M_Z values shown in Table S3, together with the results from the same calculations performed for the room temperature values.

Table S3 Calculation of the core and shell contributions to the overall saturation magnetization in core/shell nanoparticles at 5 K and 300 K according to the core and shell volumetric fraction estimated by TEM.

	M_5 K (emu/g)	*M_300 K (emu/g)*
M_F *(Fe_3O_4 core)*	98	92
M_Z *($Zn_{0.6}Fe_{2.4}O_4$ shell)*	**116(3)**	**74(2)**
M_S *(core/shell experimental data)*	109.2	81.2

The low temperature effective anisotropy of non-interacting magnetic NPs can be interpreted through the Stoner-Wohlfarth theory. If we consider NPs with blocked magnetic moments, uniaxial anisotropy and randomly distributed easy axes then the effective

anisotropy will be proportional to the coercivity according to $H_C = 0.48\frac{2 \cdot K_{eff}}{M_S}$. Then, by considering the experimental M_S and H_C values at 5 K and an average density of 5.05 g/cm^3 for the cores and 5.2 g/cm^3 for the core/shell NPs, we can estimate K_{eff} for the bare cores and the core/shell NPs, as summarized in Table S4. At room temperature, the magnetic moments are fluctuating due to the thermal energy and the NPs are in a superparamagnetic regime, hindering the possibility to estimate the anisotropy directly from the hysteresis curve. However, as shown in Table S4, we can roughly estimate the room temperature anisotropy as approximately the 75% of the low temperature value [2,3].

Table S4 Calculation of the cores and core/shell nanoparticles effective anisotropies at 5 K and 300 K.

	$\mu_0 H_C$_5 K (Oe)	K_{eff} _5 K (10^5 erg/cm^3)	K_{eff} _300 K (10^5 erg/cm^3)
cores	450	**1.9(1)**	**1.4(2)**
core/shell NPs	308	**1.8(1)**	**1.4(2)**

Simulations of the aging effects on the NP heating efficiency

The effects of the aging on the power losses can be illustrated through the linear response theory (LRT) [4], in view of the magnetic characterization of the NPs across the aging process. Our experimental results allow us to assume that fresh stoichiometric Fe_3O_4 NPs (lognormally-distributed 12.1±1.2 nm NPs with uniaxial room temperature K_{eff} = 4.5·10^5 erg/cm^3 and M_S = 347 emu/cm^3) were partially oxidized to γ-Fe_2O_3 NPs (lognormally-distributed 12.1±1.2 nm NPs with uniaxial room temperature K_{eff} = 1.4·10^5 erg/cm^3 and

M_S = 305 emu/cm^3). We assumed in the calculations that a sinusoidal magnetic field with amplitude H_{MAX}=100 Oe and f=300 kHz is applied and that the magnetization is relaxing through a purely Néel-type process (valid e.g. for immobilized NPs) given by $\tau_R = \tau_0 e^{\frac{K_{eff}V}{k_BT}}$, where τ_0=10^{-10} s, V is the volume of the NP and k_BT the thermal energy. Note that the validity of the LRT is assured under these conditions since $\mu_0 M_S H_{MAX} V/k_BT < 1$. Within this frame, the hysteresis loop area (A) is given by[4]:

$$A = \frac{\pi {\mu_0}^2 {H_{MAX}}^2 {M_S}^2 V}{3k_BT} \frac{(2\pi f\tau_R)}{1+(2\pi f\tau_R)^2}.$$

The results are summarized in Figure S3. In the upper panel, *A* is plotted as a function of the particle diameter (*D*) for both fresh and aged NPs together with the lognormal function from the size distribution analysis *f(D).* It is thus concluded that, as a result of the reduction in both the magnetization and anisotropy, the optimum size for aged cores is shifted towards larger sizes, while the optimum size for magnetite NPs according to the LRT is close to the actual size of our system. As a result, the diameter dependence of the effective areas *A·f(D)* is shown in the lower panel of Figure S3. In such case the integrated curves reflect the overall power losses of each system, which yield 0.10 mJ/g and 0.013 mJ/g for fresh and aged NPs, respectively. In sum, the aging process has a strong impact on A through both the magnetization and the effective anisotropy variations. While the decrease in the magnetization will always be detrimental to the heating efficiency, the outcome of the anisotropy variation will depend on the applied frequency and the NP size and, under certain conditions, the oxidation process might contribute to enlarge the loop area.

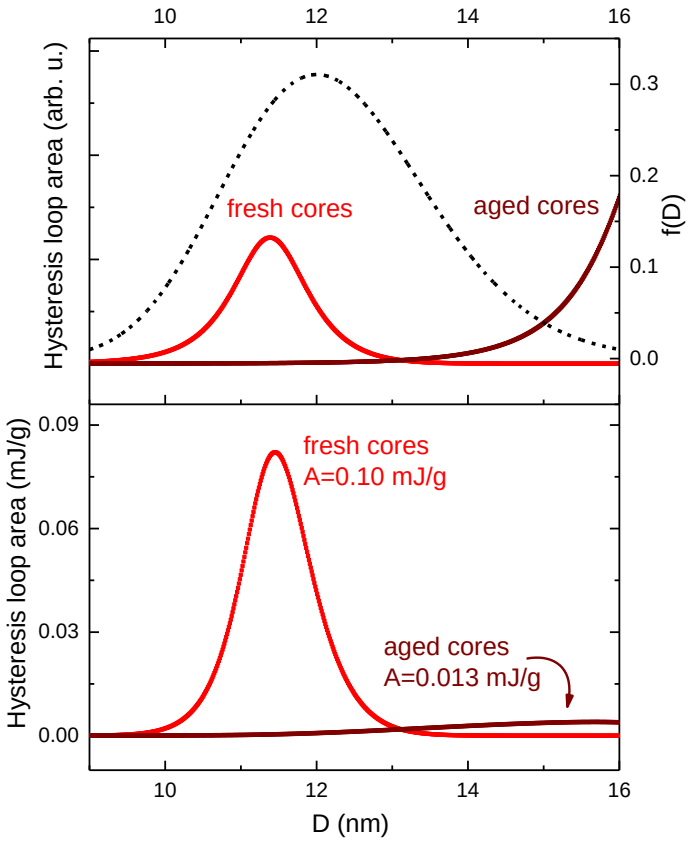

Figure S3 Upper panel: Comparison of the hysteresis loop areas predicted by the LRT (300 kHz, 100 Oe) for fresh and aged cores. Dashed lines represent the Lognormal size distribution from the structural characterization. Lower panel: effective contribution to the power losses of the calculated areas as a function of the NPs diameter.

On the other hand, the passivation effect of the shell layer is responsible for preserving K_{eff} and M_S for the core/shell NPs during the 6-month aging process and no variation in the heating efficiency is expected for such sample. It is worth noting that, due to the larger size of the core/shell NPs, the LRT is no longer valid under the same conditions (*i.e.* $\mu_0 M_S H_{MAX} V/k_B T > 1$ at H_{MAX}=100 Oe). However, a comparison of the loop areas can be performed for H_{MAX}=30 Oe, in which case the LRT conditions are simultaneously satisfied

for fresh cores, aged cores and core/shell NPs. The results are summarized in Figure S4. It is evidenced that large areas are expected for both fresh cores and core/shell samples as their experimental sizes match well the optimal sizes predicted by the theory (at 300 kHz). While this prediction holds for aged core/shell NPs, a decrease in the hyperthermia output due to the aging is, again, clearly expected for bare cores (lower panel in Figure S4). In addition, the theoretical effective area is larger for core/shell NPs due to the precise fine-tuning of the size, K_{eff} and M_S. A detailed experimental study on the heating power in this kind of core/shell NPs can be seen in Ref [5].

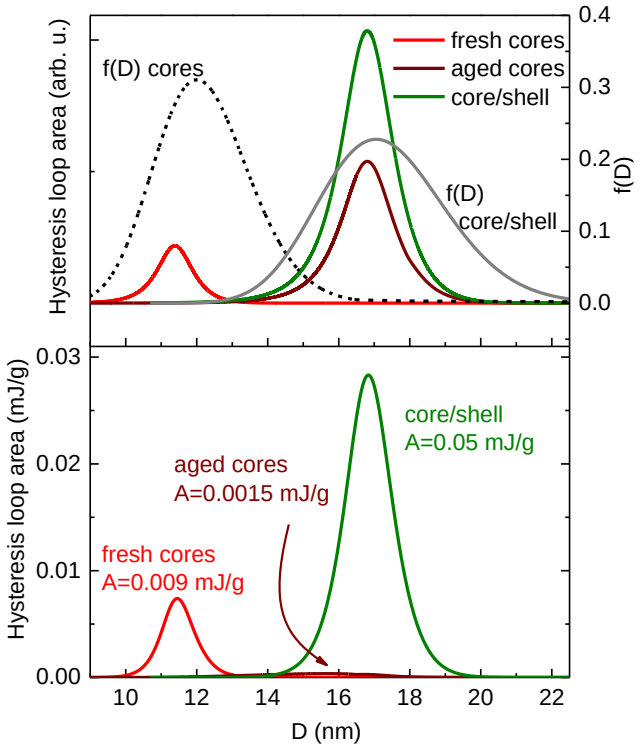

Figure S4 Upper panel: Comparison of the hysteresis loop areas predicted by the LRT (300 kHz, 30 Oe) for fresh and aged cores and core/shell NPs. Dashed and dotted lines represent the Lognormal size distribution, f(D), from the structural characterization. Lower panel: effective contribution to the power losses of the calculated areas as a function of the NPs diameter.

Estimation of the Diffusion Coefficients for Fe cations

Although our results do not allow a full exploration of the kinetics of the oxidation process, we can give an estimation of the main parameters involved. The oxidation of magnetite to maghemite is usually described through the solution to the Fick's second law for the diffusion of iron cations in a monocrystalline nanoparticle with spherical geometry, which gives [6-8]

$$\frac{\rho_t}{\rho_\infty}\frac{1}{t} = 6\pi^{-1/2}\left(\frac{D}{a^2}\right)^{1/2}\frac{1}{t^{1/2}} - 3\frac{D}{a^2}$$

where ρ_t and ρ_∞ are the fraction of diffused iron cations after a time t and infinite time, respectively, D is the diffusion coefficient and a is the radius of the magnetite core; in addition, $\frac{\rho_t}{\rho_\infty}$ also represents the fraction of maghemite formed after a time t. In Figure S5 we calculated the expected values of $\frac{\rho_t}{\rho_\infty}$ as a function of time for different diffusion coefficients.

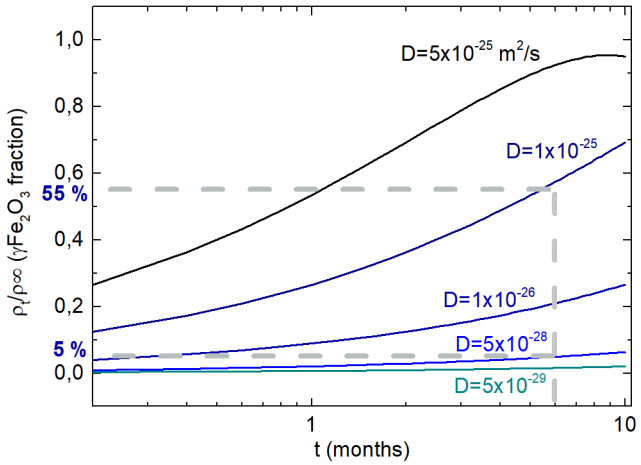

Figure S5 Maghemite fraction as a function of the time for different diffusion coefficients. The experimental maghemite fractions fore aged cores (55 %) and the upper bound for the maghemite fraction in core/shell NPs (5%) are indicated with dashed lines**.**

From the calculated curves it is possible to estimate the diffusion coefficients associated to the formation of a certain maghemite fraction in the structure. According to the model, a 55% of maghemite (as found in our aged bare cores) would correspond to a diffusion coefficient of $D \approx 1 \cdot 10^{-25}$ m^2/s, the same order of magnitude although lower than ref. [9]. In the case of the core/shell NPs, as we observed a stoichiometric magnetite core, we are able to estimate an upper bound for the diffusion coefficient by taking into account the error of the magnetite fraction obtained from the Mössbauer spectra (around 5 %). Therefore, as shown in Figure S5, the diffusion coefficient for the magnetite in the core/shell structure is $D < 5 \cdot 10^{-28}$ m^2/s, which is two orders of magnitude lower than the estimation for the bare cores.

References

[1] Coey, J. M. D. *Magnetism and Magnetic Materials*; Cambridge University Press, 2010.

[2] Shenker, H. Magnetic anisotropy of cobalt ferrite ($Co_{1.01}Fe_{2.00}O_{3.62}$) and nickel cobalt ferrite ($Ni_{0.72}Fe_{0.20}Co_{0.08}Fe_2O_4$). *Physical Review* **1957**, 107(5), 1246.

[3] He, S.; Zhang, H.; Liu, Y.; Sun, F.; Yu, X.; Li, X.; Zhang, L.; Wang, L.; Mao, K.; Wang, G.; et al. Maximizing Specific Loss Power for Magnetic Hyperthermia by Hard–Soft Mixed Ferrites. *Small* **2018**, 14 (29). https://doi.org/10.1002/smll.201800135.

[4] Carrey, J.; Mehdaoui, B.; Respaud, M. *J. Appl. Phys.* **2011**, 109, 083921

[5] Lavorato, G.C.; Das, R.; Xing, Y.; Robles, J.; Litterst, F. J.; Baggio-Saitovitch, E.; Phan M.H.; Srikanth, H. *ACS Appl. Nano Mater.* **2020** 3(2), 1755-1765. http://doi.org/10.1021/acsanm.9b02449

[6] Sidhu, P. S.; Gilkes, R. J.; Posner, A. M. Mechanism of the Low Temperature Oxidation of Synthetic Magnetites. *J. Inorg. Nucl. Chem.* **1977**, 39 (11), 1953–1958. https://doi.org/10.1016/0022-1902(77)80523-X.

[7] Tang, J.; Myers, M.; Bosnick, K. A.; Brus, L. E. Magnetite Fe 3 O 4 Nanocrystals: Spectroscopic Observation of Aqueous Oxidation Kinetics. *J. Phys. Chem. B* **2003**, 107 (30), 7501–7506. https://doi.org/10.1021/jp027048e.

[8] Bourgeois, F.; Gergaud, P.; Renevier, H.; Leclere, C.; Feuillet, G. Low Temperature Oxidation Mechanisms of Nanocrystalline Magnetite Thin Film. *J. Appl. Phys.* **2013**, 113 (1). https://doi.org/10.1063/1.4772714.

[9] Bogart, L. K.; Blanco-Andujar, C.; Pankhurst, Q. A. Environmental Oxidative Aging of Iron Oxide Nanoparticles. *Appl. Phys. Lett.* **2018**, 113 (13). https://doi.org/10.1063/1.5050217 .